Ahmed Kord and Andrea Alù

Magnetless Circulators Based on Synthetic Angular-Momentum Bias

Recent advances and applications.

In this article, we discuss recent progress in magnet-free nonreciprocal structures based on a synthetic form of angular-momentum bias imparted via spatiotemporal modulation. We examine how such components can support metrics of performance comparable to traditional magnetic-biased ferrite devices, while at the same time offering distinct advantages in terms of reduced size, weight, and cost due to the elimination of magnetic bias. We further provide an outlook on potential applications and future directions based on these components, ranging from wireless full-duplex communications to metasurfaces and topological insulators (TIs).

INTRODUCTION

The demand for multimedia-rich applications and services has been dramatically increasing over the last few decades. As a result, the sub-6-GHz electromagnetic spectrum, where most deployed communication systems operate, has become saturated with unprecedented data traffic, leaving no more bandwidth (BW) for further growth in the transmission rate. To overcome this problem, full-duplex radios have been proposed. In such systems, data streams are transmitted in the uplink and downlink simultaneously on the same carrier frequency [1]–[9], which doubles the spectral efficiency compared to half-duplex time- and frequency-division systems. The key challenge in full duplexing, however, is that it requires considerably large self-interference cancellation (SIC) between the transmitter (Tx) and receiver (Rx) of every communication node to prevent the strong Tx signal from saturating the Rx front-end modules. For instance, Wi-Fi signals are transmitted at an average power of +20 dBm and the noise floor is approximately –90 dBm, hence, SIC is required to be as high as +110 dB. For many years, this level of SIC was impossible to attain; therefore, full-duplex radios were presumed irrelevant in practice.

Recently, several works have challenged this long-held assumption and demonstrated that full duplexing can, in fact, be achieved by using a combination of radio-frequency (RF) [3]–[5], analog [6], [7], and digital techniques [8], [9]. The basic idea in digital and analog approaches is to generate a weighted version of the Tx signal that mimics its echo into the Rx and subtract it from the Rx signal before and after the analog-to-digital converter. Because the strength contrast between the Tx and Rx signals can be billions of magnitude, the subtraction must be performed extremely accurately, otherwise, it may

Digital Object Identifier 10.1109/MAP.2020.3043437
Date of current version: 4 January 2021

end up adding more interference. But the presence of nonidealities such as noise, nonlinearity, and dynamic variation of the antenna (ANT) input impedance make this process a nontrivial task. Therefore, analog and digital SIC approaches must be preceded by another layer of isolation (IX) at the RF front end to relax their design requirements and mitigate their sensitivity to inevitable errors. Fortunately, circulators can play this role [10]–[64]. Not only can they achieve low insertion loss (IL), thus overcoming the fundamental limit of electrical-balance duplexers, but they also allow the Tx and Rx nodes to share a single ANT, which makes full duplexing more attractive compared to multiple-input, multiple-output radios.

For decades, circulators have been built almost exclusively through the magnetic biasing of rare-Earth ferrites [10]–[19]. These magnetic devices can achieve excellent performance in terms of IX, power handling, BW of operation, and IL, yet they typically result in bulky, nonintegrable, and expensive devices that may not be suited for various commercial systems. To overcome these problems, magnet-free implementations of circulators based on active solid-state devices or nonlinear materials with geometric asymmetries have been pursued [20]–[29]. Despite significant research efforts over many years, these alternative solutions continued to suffer from a fundamentally poor noise figure (NF), nonlinearities and limited power handling, hence the appeal of a fully passive magnet-free material that can operate on par, or even outperform magnetic approaches.

Recently, however, it was shown that parametric circuits can overcome these limitations and achieve excellent performance, together with fewer costs and smaller sizes. For example, the authors in [31] introduced the concept of spatiotemporal modulation angular-momentum (STM-AM) biasing to synthesize cyclic-symmetric magnetless circulators. This was then followed by numerous works extending these concepts to realize various magnet-free components, including circulators, gyrators, and isolators [31]–[55]. In particular, the authors in [33]–[36] refined the STM-AM concept by finding the necessary conditions to ideally mimic magnetic-biased cavities, thus enabling the development of many new circuits with unprecedented performance. In this article, we review recent advances in STM-AM devices and provide an outlook of their possible impact on technology and future research directions. We also discuss the unusual properties of 2D metasurfaces consisting of arrays of such elements, which may be engineered to behave as magnetized ferrites or TIs [66]–[85].

OPERATION PRINCIPLES OF MAGNETIC CIRCULATORS

The scattering (S)-matrix of an ideal circulator can, in general, be written in the following form:

$$\bar{\bar{S}} = \begin{bmatrix} 0 & 0 & 1 \\ 1 & 0 & 0 \\ 0 & 1 & 0 \end{bmatrix}. \tag{1}$$

Equation (1) shows that an input signal at, say, port 1, is exclusively routed to port 2 without any reflections or leakage to port 3. Similarly, an input signal at ports 2 or 3 is routed to ports 3 and 1, respectively. In other words, an ideal circulator is cyclic symmetric and exhibits zero IL, perfect matching, and infinite IX. In reality, however, not only is the S-matrix limited by inevitable dissipation in the constituent materials of the circulator, but it is also frequency dispersive and maintains nonreciprocity over a finite BW. Despite such practical imperfections, the harmonic response of a linear, nondispersive cyclic-symmetric circulator can still give us an invaluable insight into the physical principles of breaking reciprocity. For example, an excitation at one port of an ideal circulator, say, port 1, can be decomposed using superposition in three subcircuits, as shown in Figure 1(a)–(c).

In Figure 1(a), the applied voltage sources are identical in both magnitude and phase, while in Figure 1(b) and (c), the sources have different phases, which increase by 120° in either the clockwise or counterclockwise direction. Because of such distinctive phase patterns, we refer to such excitations as the *in-phase* (*0*), *clockwise* (+), and *counterclockwise* (–) modes, respectively. In general, each of these modal excitations generates a current component at the output ports, and their linear combination gives the solution to the original excitation at port 1. If the circuit is symmetric and has only three terminals (no internal connections to ground), then a nonzero in-phase current violates Kirchhoff's current law, hence, it cannot be excited. Furthermore, if a preferred sense of precession is provided to the counterrotating currents, then they will be excited with an equal amplitude, say, I_g, and opposite phase, say, $\pm\alpha$. Consequently, the total current at the nth port becomes

$$I_n = 2I_g \cos\left((n-1)\frac{2\pi}{3} + \alpha\right), \tag{2}$$

where n is the port index. For $\alpha = 30°$, (2) results in $I_3 = 0$ and $I_1 = -I_2 = \sqrt{3}\, I_g$. In other words, the impinging signal at port 1 is exclusively routed to port 2 and isolated from port 3. This implies that it is possible to implement an ideal circulator by imparting a preferred sense of precession to a pair of counterroting modes in a symmetric, three-port network.

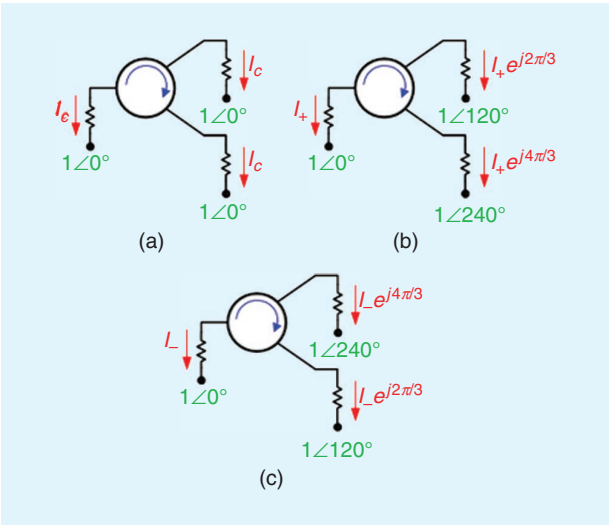

FIGURE 1. The eigenmodes of a generic three-port circulator [35]. (a) The in-phase mode, (b) the clockwise mode, and (c) the counterclockwise mode.

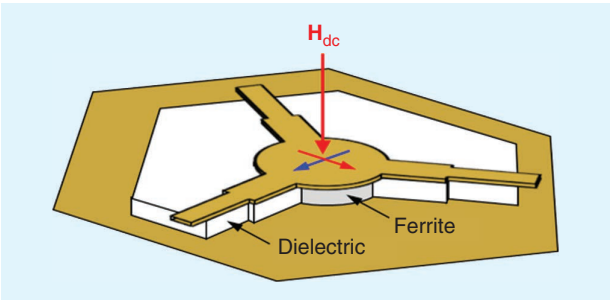

FIGURE 2. A stripline Y-junction magnetic circulator [10].

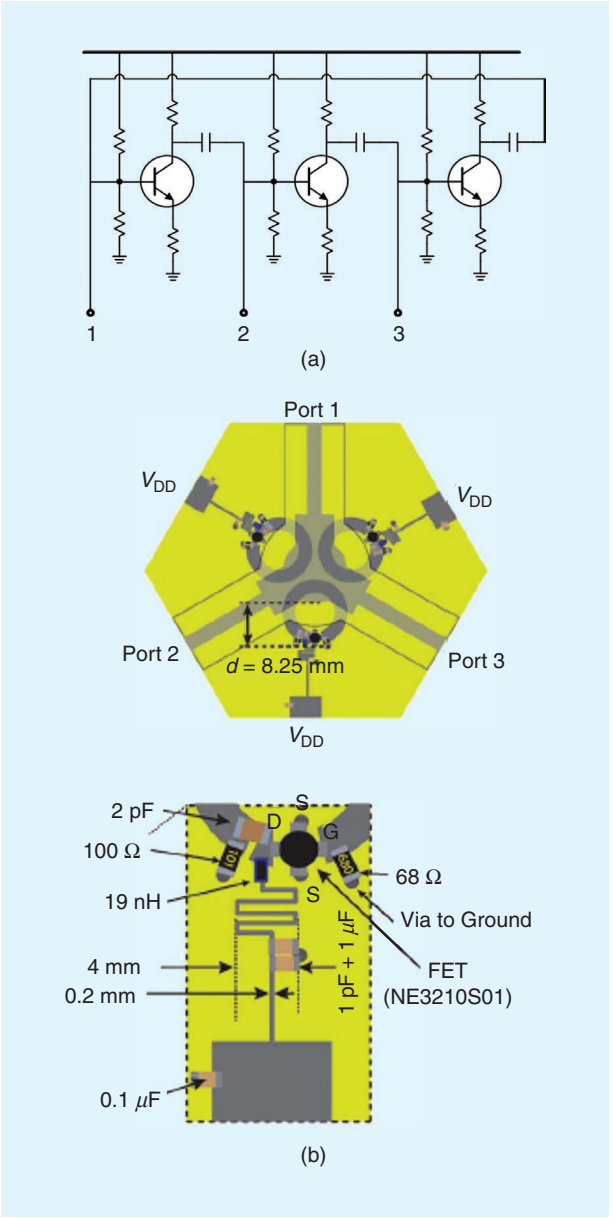

FIGURE 3. (a) An active circulator consisting of three common-emitter amplifiers in a loop, each acting as an isolator [20]. (b) An active circulator consisting of three coupled transistor-loaded ring resonators forming an artificial metamaterial nonreciprocal core [22].

This principle indeed governs the way in which magnetic circulators operate: Consider a ferrite cavity connected symmetrically to three ports at 120° intervals, as depicted in Figure 2. If a strong magnetic bias is applied orthogonally to the cavity to align the spinning electron dipole moments along a particular direction, the spin imparts a form of angular-momentum bias at the microscopic level, which, in turn, translates into a preferred sense of precession for the rotating modes of the cavity. As a result, if these modes are excited by an impinging signal at one port, say, port 1, they accumulate different phases as they appear at the other two ports. For a particular strength of the bias, these modes can sum up in phase at one of the output ports, i.e., port 2, and destructively interfere at the other, i.e., port 3. If power dissipation inside the cavity is negligible, it means that the incident power is exclusively routed from port 1 to 2. Due to the geometrical threefold symmetry of the circulator, excitation at ports 2 or 3 will similarly be routed to ports 3 and 1, respectively, which yields the S-matrix of (1).

LIMITATIONS OF ACTIVE CIRCULATORS

Despite the fact that magnetic circulators can achieve excellent *S*-parameters, power handling, and noise performance with negligible power consumption, they suffer from a large size and high cost due to the fact that they require an external bulky magnet and rare-Earth ferrite materials. These critical problems prohibited an ubiquitous use of such devices in wireless communication systems and played an important role in consolidating the false assumption that full-duplex radios are impossible to realize in practice. For this reason, an interest in investigating magnet-free approaches to design circulators has emerged since the advent of solid-state transistors. When a transistor, for instance, is biased with a dc current, it operates as a transconductance amplifier, which converts ac voltages applied at its base terminal into large currents flowing from its emitter to collector terminals. A reverse voltage applied at either of the output terminals, however, is isolated from the base. In other words, a current-biased transistor operates as an isolator with forward gain. By combining three such active isolators in a loop, as shown in Figure 3(a), an active magnet-free circulator can be constructed, as explained in [20].

The variants of these circuits at different frequency ranges were also investigated over the years. For example, a robust, low-frequency implementation using operational amplifiers was also presented in [21]. More recently, a synthetic, active metamaterial consisting of an array of transistor-loaded microstrip ring resonators was also proposed in [22] as an artificial medium to replace magnetic-biased ferrites. In such materials, the transistors simply kill one of the rotating modes supported by the ring, thus allowing the realization of active circulators, as depicted in Figure 3(b).

It is also worth mentioning that nonlinear materials have also been explored as an alternative medium to realize magnet-free circulators, especially at optical frequencies where transistors do not exist [27]–[29]. However, the resulting devices were able to work when only one port was excited at a time. When two or more ports are concurrently excited, the *S*-parameters

suffer from hysteresis and strongly depend on the relative phase among the input signals. Therefore, this approach is less useful than its active transistor-based counterpart, which can support simultaneous excitation from different ports, and at the same time offers distinct advantages in terms of weight, size, cost, and scalability compared to magnetic-biased ferrite devices. Unfortunately, however, active circulators still suffer from low power handling and a poor NF. A comprehensive analysis of these fundamental limitations was presented in [26], leading to the conclusion that active circulators are not suitable for use as front-end modules in the vast majority of microwave applications where either the Tx power is high or the Rx sensitivity is critical.

PARAMETRIC STM-AM CIRCULATORS

In recent years, time-varying circuits were presented as a promising solution to realize circulators that could handle much higher power, exhibit better linearity, and achieve a lower NF than active implementations, while at the same time eliminating the necessity for bulky magnets and expensive materials needed in ferrite devices. Table 1 summarizes these advantages in comparison to traditional magnetic and active technologies presented in previous sections.

Among all of the recent works on parametric circulators, STM-AM circuits, which are the main focus of this article, have shown significant promise in satisfying the challenging requirements of practical systems at different portions of the electromagnetic spectrum. In particular, in [56], our group presented a circulator for airborne sound by synthesizing an effective angular-momentum bias in the form of the mechanical rotation of air inside a circularly symmetric resonant acoustic cavity. Such biases have imparted a macroscopic sense of precession to the degenerate modes of opposite handedness supported by the cavity, which translates into nonreciprocity and IX, as explained in the "Operation Principles of Magnetic Principles" section. Using similar principles, one could imagine spinning a circuit board sufficiently fast to break reciprocity for the electromagnetic signals traveling across a resonant device, but arguably, this mechanical spin would be even less practical than the magnetic approaches to nonreciprocity. However, spatiotemporal modulation can impart a form of synthetic angular-momentum bias, enabling the implementation of compact STM-AM circulators as described in the following.

TABLE 1. A COMPARISON AMONG DIFFERENT CIRCULATOR DESIGN APPROACHES.

Approach	Magnetic	Active	Parametric
Magnet	Required	Not required	Not required
Size	Large	Small	Medium
Cost	High	Low	Low
IL	Low	Low (or gain)	Medium
IX	Medium	Medium	High
BW	Wide	Average	Average
Power handling	High	Low	Medium
NF	Low	High	Medium
Power dissipation	Low	High	Medium

SINGLE-ENDED TOPOLOGIES

Consider a symmetric-resonant three-port network consisting of three series or parallel inductance–capacitance (LC) tanks connected in a loop or to a central node resulting in four possible combinations, as shown in Figure 4. Let us further assume that the instantaneous oscillation frequencies of the tanks are spatiotemporally modulated as

$$f_n = f_0 + \Delta f \cos\left(2\pi f_m t + (n-1)\frac{2\pi}{3}\right), \quad (3)$$

where $f_0 = 1/2\pi\sqrt{L_0 C_0}$ is the natural oscillation frequency of the tanks, Δf is the modulation depth, and $f_m = \omega_m/2\pi$ is the modulation frequency. In practice, (3) is implemented using varactors, switched capacitors, or Josephson junctions (depending on the target application). In the case of varactors, for instance, Δf can be written as $\Delta f = kV_m$, where k is the slope of the capacitance-voltage curve. The modulation scheme of (3) synthesizes an effective angular-momentum bias in the clockwise direction because the phases of the modulation signals increase by 120° in that direction, thus lifting the degeneracy

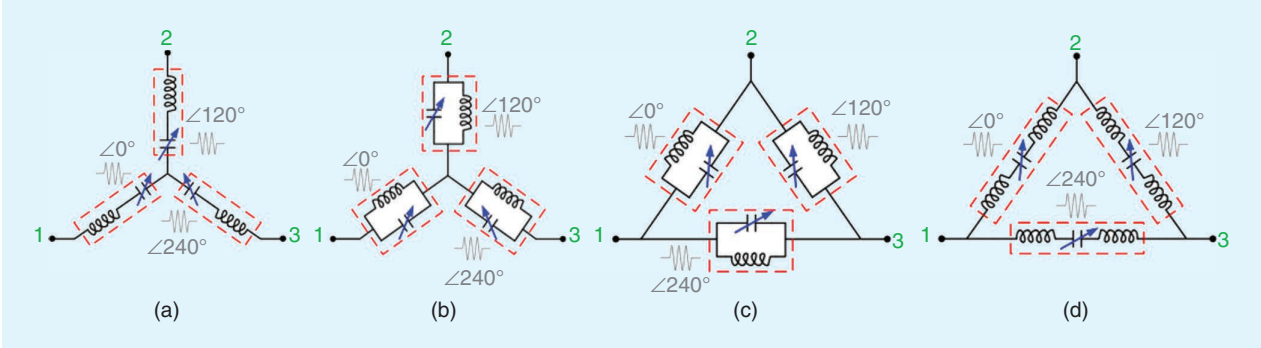

FIGURE 4. The single-ended topologies of STM-AM circulators [35]. (a) Bandpass/wye, (b) bandstop/wye, (c) bandstop/delta, and (d) bandpass/delta.

of the rotating modes and allowing them to oscillate at different frequencies, say, $\omega_{\pm}$.

Between these two frequencies, the skirts of the resonances do allow for transmission, whether the original resonance was bandpass or bandstop, and they exhibit opposite phases. Therefore, if an input signal is incident at one port in the middle of these two frequencies, i.e., at ω_0, it will excite the two resonances with equal magnitude and opposite phases $\pm\alpha$, which is consistent with the generic description of the previous section based on providing a preferred sense of precession. It is also worth mentioning that the amount of splitting $\omega_+ - \omega_-$ depends on the modulation parameters f_m and V_m, thus allowing for control of the value of α. As explained previously, for $\alpha = 30^\circ$, ideal circulation can be achieved at ω_0. In light of this discussion, this condition will correspond to a certain combination of f_m and V_m.

As an example, the bandstop/delta topology displayed in Figure 4(c) was built and tested in [33]. The measured IL, return loss (RL), and IX at the center frequency of 1 GHz were 3.3, 10.8, and 55 dB, respectively, and the measured BW was 2.4% (24 MHz). This circuit can also be reconfigured for operation at different channels over a frequency range of 60 MHz by simply changing the dc bias of the varactors. The measured 1- and 20-dB compression points of the IL and IX, respectively, were both +29 dBm. Also, the measured input-referred third-order intercept point (IIP3) was +33.8, which are reasonable nonlinearity metrics meeting the specifications for a range of applications. It is important to stress that these metrics stem from the properties of the employed circuit components, not from a fundamental limit in the approach to nonreciprocity. It can also be proven that STM-AM circulators are inherently passive linear circuits [42], hence we expect that the overall NF is approximately equal to the IL but slightly larger due to noise folding from the intermodulation products (IMPs) and phase noise in the modulation signals. Indeed, the measured NF was 4.5 dB at 1 GHz and less than 4.7 dB over the BW. These results are summarized in Table 2, and the interested reader is referred to [33] for further technical details.

DIFFERENTIAL CONFIGURATIONS

As mentioned in the previous section, single-ended STM-AM circulators can achieve good performance in terms of several metrics, particularly in terms of power handling and NF. Nevertheless, these circuits suffer from large IMPs in close proximity to the desired BW resulting from parametric mixing induced by the temporal modulation and from the inevitable nonlinearities associated with its circuit components. These IMPs draw power from the input signal, which limits the IL to roughly 2 dB in practice. They are also considerably large, i.e., only 10 dB below the fundamental harmonic, and they equally appear at all ports for excitation at a single port. Therefore, the IMPs resulting at the Rx port from the Tx excitation could saturate the Rx front end regardless of how much IX is achieved at the fundamental frequency. Similarly, the IMPs resulting from the Rx signal

TABLE 2. A SUMMARY OF THE MEASURED RESULTS IN COMPARISON TO PREVIOUS WORKS.

Reference	[33]	[34]	[35]¥	[36]	[37]	[41]
Architecture	Single-ended bandstop/delta	Differential bandstop/delta	Parallel *N*-way bandstop/delta	Broadband current-mode bandpass/wye	Current-mode bandpass/wye	Current-mode bandpass/wye
Technology	PCB	PCB	N/A	PCB	CMOS 180 nm	MEMS/PCB
Center frequency (GHz)	1	1	1	1	0.91	2,500
Modulation frequency (%)	19	10	10	11	11.6	1.6
20-dB IX BW (%)	2.4	2.3	3	14	2.4	0.72
Maximum IX (dB)	55	24	25	31	65	30
Minimum IL (dB)	3.3	0.8†	2.2	4.2	4.8	4
Maximum RL (dB)	11	23	24	16.7	11	15
P1 dB (dBm)	+29	+29	+39	+23	N/A	+28
IX 20 dB (dBm)	+29	+28	+41	N/A	N/A	N/A
IIP3 (dBm)	+33	+32	+43	N/A	+6	+40
Minimum NF (dB)	4.5	2.5	2.2	N/A	5.2	N/A
Maximum IMP (dBc)	–11 at $f_0 \pm f_m$	–30 at $f_0 \pm f_m$	–62 at $f_0 \pm 2f_m$	–22 at $f_0 \pm f_m$	–20 at $f_0 \pm f_m$	–30 at $f_0 \pm f_m$
Power dissipation (MW)	N/A	N/A	N/A	N/A	64	0.15
Size (mm^2)	143	286	N/A	480	36	225*

PCB: printed circuit board; MEMS: microelectromechanical systems; N/A: not available; ¥: simulation results; †: baluns are de-embedded; MEMS die area = 0.25 mm^2.

at the Tx port can cause instability issues to the power amplifier because of load-pull effects. More importantly, the IMPs at the ANT port, due to either the Tx or Rx signal, pose a serious interference problem to adjacent channels and would prohibit compliance with the spectral mask regulations of most commercial systems. Therefore, it is crucial to reject these products. This problem was overcome in [34] by combining two single-ended circuits similar to those presented in the previous section in a differential voltage- or current-mode architecture, as shown in Figure 5, and by maintaining a constant 180° phase difference among their modulation signals, i.e.,

$$f_{n,\pm} = f_0 \pm \Delta f \cos\left(2\pi f_m t + (n-1)\frac{2\pi}{3}\right), \quad (4)$$

where $f_{n,+}$ and $f_{n,-}$ are the modulation signals of the two constituent single-ended circuits. As an example, in [34], the voltage-mode configuration of Figure 5(b) was built and tested using two of the single-ended bandstop/delta circuits depicted in Figure 4(c). The measured IL, RL, and IX after de-embedding the baluns were 0.78, 23, and 24 dB, respectively, and the fractional BW was 2.3% (23 MHz). Table 2 also summarizes these results along with other metrics, and the interested reader is referred to [34] for further details.

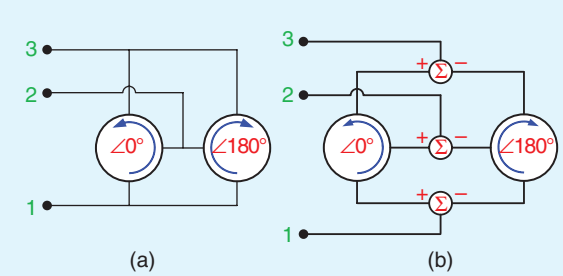

FIGURE 5. The differential configurations of STM-AM circulators [34]. (a) The current mode and (b) the voltage mode.

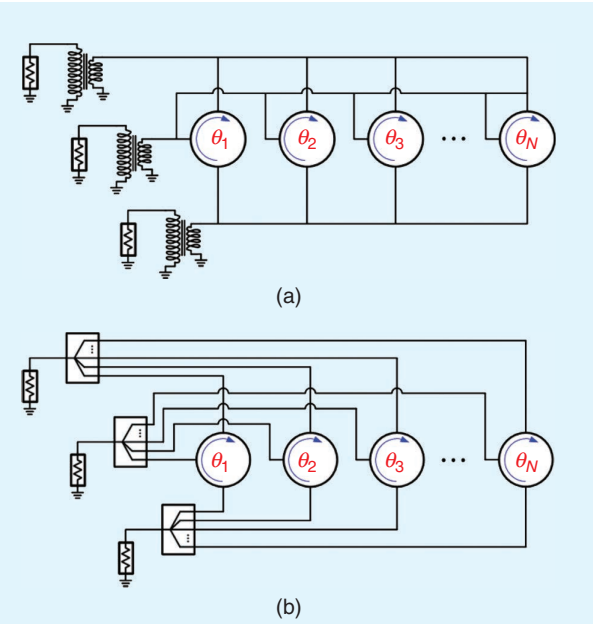

FIGURE 6. *N*-way architectures of STM-AM circulators [35]. (a) The parallel interconnection based on a current combination. (b) The series interconnection based on a voltage summation.

N-WAY ARCHITECTURES

Although the differential STM-AM circulators presented in the previous section dramatically improved performance over many metrics compared to the single-ended implementations, their spurious emission can remain strong when nonidealities in the circuit are considered. To address this problem, we can extend the differential configuration to an *N*-way architecture consisting of *N* unit cells connected in parallel or in series, as presented in Figure 6 [35]. The modulation scheme in this case becomes

$$f_{ni} = f_0 + \Delta f \cos\left(2\pi f_m t + (n-1)\frac{2\pi}{3} + (i-1)\frac{2\pi}{N}\right), \quad (5)$$

where $i = 1{:}N$ is the unit index and $n = 1{:}3$ is the tank index in the ith unit. Equation (5) reduces to (4) for $N = 2$, and this generalization is more effective at eliminating the IMPs that are not multiples of Nf_m in the presence of nonidealities, such as nonlinearities, phase-synchronization errors, and random mismatches among the constituent elements. As a by-product, *N*-way circulators provide better power handling, enhanced by a factor of *N* because the input power is split among *N* units. Nonetheless, the benefits of *N*-way architectures come at the expense of an overall increased size and power consumption. As mentioned previously, Table 2 lists the results, and the interested reader is referred to [35] for further technical details.

BW EXTENSION

The instantaneous BW of all the circuits presented thus far is limited by the modulation frequency f_m, the loaded quality (Q) factor Q_l of the resonant junction, and the order of the constituent resonators. For example, first-order resonators, i.e., series or parallel *LC* tanks, with ~10–20% modulation frequency and a 50-Ω termination led to a BW of roughly ~3–4% at best. One solution to improve this further is to increase f_m, but this approach increases power consumption, prohibits the use of thick-oxide low-speed technologies that could handle high power, and complicates scaling the center frequency to the millimeter-wave bands. Alternatively, one may think of replacing the *LC* tanks with high-order *LC* filters, but this would increase the circuit complexity and size dramatically.

In [36], an optimal solution based on terminating a narrowband circulator with three identical bandpass filters, as depicted in Figure 7, was proposed. The added filters are essentially matching networks that shape the frequency of the combined network and maintain a certain level of IX over a wider BW. A theoretical bound on the maximum-possible BW for a given modulation frequency was also derived in [36]. As one may expect, to approach such a bound, the order of the matching filters must be very large. In practice, however, the maximum order is limited by the additional losses exhibited by the filters themselves, which

increase the circulator's overall IL. To experimentally validate this technique, the authors in [36] relied on a second-order filter and a current-mode bandpass/wye STM-AM circuit, resulting in a three-fold increase in the BW from 4% (40 MHz) to 14% (140 MHz). The measured results of all the other metrics are summarized in Table 2; see [36] for further details.

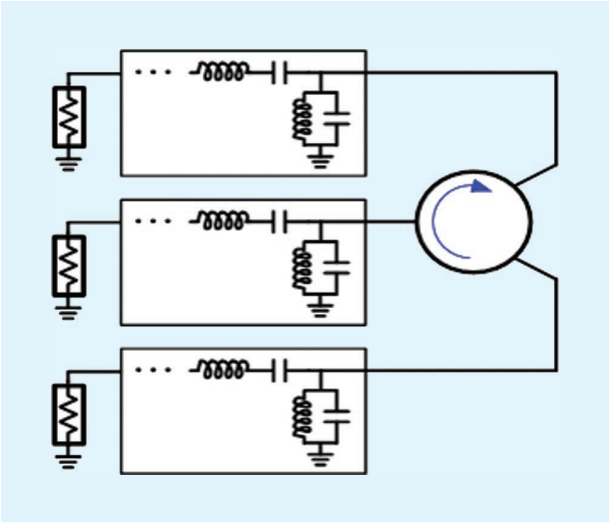

FIGURE 7. The BW extension of STM-AM circulators based on terminating the ports of a narrow-band differential or *N*-way circuit with three properly designed matching filters.

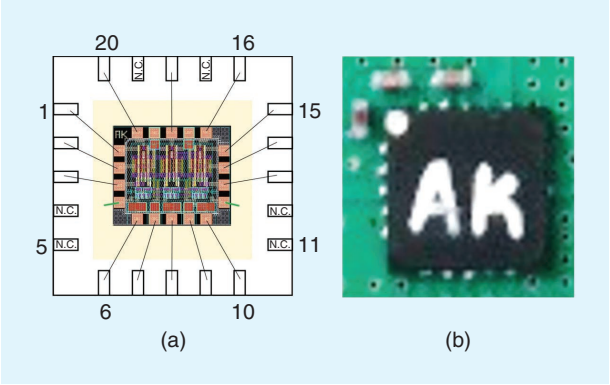

FIGURE 8. Photos of the first CMOS STM-AM circulator [37]. (a) A chip and (b) a board.

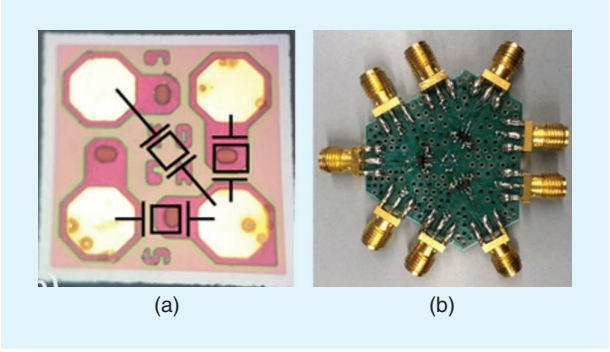

FIGURE 9. Photos of the first MEMS STM-AM circulator [41]. (a) A chip and (b) a board.

INTEGRATED IMPLEMENTATIONS

The results presented in the previous sections were all based on printed circuit board (PCB) prototypes, which, despite outperforming previous works in many metrics, were still limited in size. To overcome this problem and to achieve significant miniaturization, an integrated circuit implementation is highly desirable. Toward this goal, Kord et al. [37] modified the bandpass/wye topology of Figure 4(a) to be compatible with CMOS technologies and experimentally validated the resulting circuit in a current-mode architecture using a 180-nm process. In particular, the modulated capacitors were implemented using switched capacitors, which resulted in a larger modulation index than varactors, alleviated the tradeoff between the index and the Q factor, and permitted the use of digital clocks (which can be easily generated on chip).

Figure 8 displays photos of the fabricated chip and the testing board presented in [37]. It is also worth mentioning that this was the first CMOS implementation of STM-AM circulators ever presented. The measured RL, IL, and IX at the center frequency of 910 MHz were roughly 12, 4.9, and 60 dB, respectively. Also, the measured IIP3 was +6 dBm, which was limited by the electrostatic discharge protection circuitry, and the NF was 5.2 dB. Similarly, these results are all summarized in Table 2; see [37] for further details.

Although a CMOS implementation of STM-AM circulators does indeed significantly reduce the size compared to a PCB design, extreme miniaturization is still limited by the fact that on-chip inductors consume a large silicon area and exhibit low Q factors. This problem can be overcome by using micromachined integrated devices, such as microelectromechanical systems (MEMS) resonators. Such devices can exhibit a series resonance with a very high Q factor, which mimics the response of a series LC tank while being much smaller in size. However, MEMS resonators also suffer from a parasitic parallel resonance in close proximity to its series resonance. For devices operating in the low-GHz range, the parasitic resonance can be shifted to higher frequencies with a small inductor of ~0.5–1 nH, which can be realized using a bondwire, thus maintaining the benefit of reducing the circulator's area. As an example, Yu et al. [41] presented the first MEMS implementation of STM-AM circulators, as depicted in Figure 9. The measured RL, IL, and IX at the center frequency of 2.5 GHz were roughly 15, 4, and 30 dB, respectively.

A distinct advantage of MEMS implementations is also manifested by the fact that they allow a significant reduction of the modulation frequency. In this design, the modulation frequency was as small as 40 MHz (1.6%) which resulted in a very low power consumption of only 150 μW. However, this advantage comes at the expense of a narrow-band BW which was about of 18 MHz (0.72%). These results are summarized in Table 2; see [41] for further details.

METAMATERIAL APPLICATIONS

The applications of the STM-AM concepts presented thus far have been heavily investigated over the last few years. Although full-duplex communication is an obvious example, as explained

previously in this article, other applications have also been explored. Specifically, in the field of metamaterials, STM-AM biasing has recently been exploited to synthesize Faraday rotation for free-space propagating waves hitting a metasurface formed by arrays of such elements and for the topological phenomena for surface-wave propagation along such arrays. A magneto-optical material biased by a dc magnetic field supports circular birefringence and Faraday rotation, which may be used as a way to realize nonreciprocal wave propagation for free-space radiation.

Similarly, an array of STM-AM elements like those described in previous sections of this article can impart circular birefringence over a thin surface, causing Faraday rotation to a linearly polarized impinging plane wave that may be directly translated into the implementation of free-space isolators [30]. The nonreciprocal polarization rotation imparted by such metasurfaces can reach thousands of degrees per wavelength, a very impressive metric considering that these surfaces can be implemented in standard CMOS technology without the need for an applied magnetic bias. Beyond the electro-optical modulation of these arrays, similar phenomena can be achieved using an all-optical modulation via nonlinearities. By parametrically pumping a nonlinear etalon with two circularly polarized waves at detuned frequencies, it is possible to impart an effective angular-momentum bias that replaces the modulation schemes discussed in previous sections [65].

Opportunities have also arisen to impart nonreciprocal responses to surface waves propagating along an array of STM-AM biased devices. Arguably, a striking example of this type is the opportunity to mimic the response of a TI for electromagnetic waves. A TI is a material that acts as an insulator in the bulk and as a conductor on its edge or boundary, independent of the way in which the boundary is deformed or changed [66]–[69]. What makes these materials unique is that their edge-conduction states are symmetry protected by the topology of their conduction bands delimiting the bandgap, hence they allow unusually robust conduction properties at the foundations of the quantum Hall effect, among many other unusual phenomena. Translating these concepts from electronics to electromagnetics, a photonic TI enables unidirectional, reflection-free propagation on the edges of the (meta)material within a photonic bandgap, which is immune from a wide range of structural imperfections. The existence of such modes can be directly predicted from the topology of the bands of an infinite lattice by calculating the so-called topological invariant, a quantity that describes the nature of the bandgap boundaries in momentum-frequency space. If the topological invariant of the bands delimiting the bandgap are different, then the bandgap necessarily supports a boundary mode, which is inherently topologically protected from disorder and back reflections.

Although TIs were originally envisioned and discovered in condensed-matter physics, their extension to classical photonics [69]–[78], acoustics [79]–[83], and circuits [83]–[85] has driven considerable excitement. In such a case, symmetry breaking at a degeneracy point in momentum space is typically sufficient to induce topological order and enable edge states. Breaking time-reversal symmetry is a particularly effective way to realize electromagnetic TIs because it supports robust, broadband nonreciprocal propagation and guarantees the absence of reflected modes regardless of the nature of the possible disorder in the system.

Here we consider an array of STM-AM elements that realize an electromagnetic TI with nonreciprocal edge propagation. Because the edge states in this case emerge from periodic temporal variations, the resulting system is referred to as a *Floquet TI*. An example is shown in Figure 10(a) [81], where the unit cell of the corresponding hexagonal lattice is depicted in Figure 10(b), and it consists of two waveguide STM-AM circulators

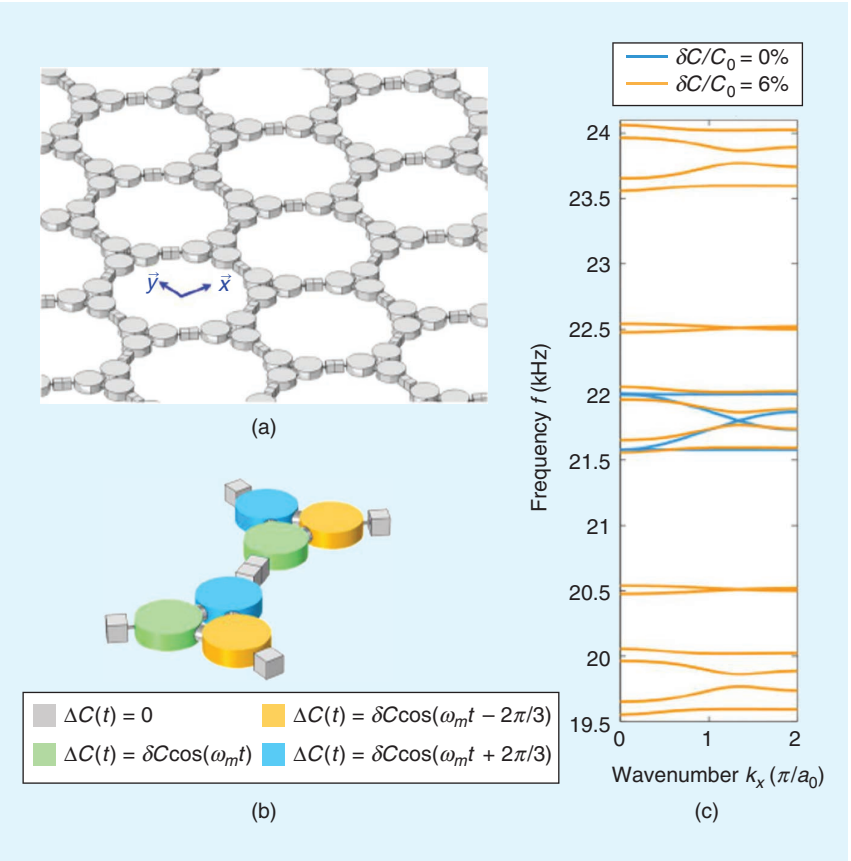

FIGURE 10. (a) The hexagonal lattice consisting of acoustic STM-AM circulators, forming a Floquet TI for sound waves [81]. (b) A unit cell consisting of two acoustic STM-AM circulators. (c) A comparison between the band structure of an infinite lattice with and without modulation, showing a band gap opening in the vicinity of 22 MHz when modulation is turned on.

in which the time modulation synthesizes a rotation, similar to what was described in the previous sections, to impart an effective angular-momentum bias. The STM-AM waveguide circulator is consistent with the bandpass/delta topology of Figure 4(d), and the modulation can be achieved by modulating the volume of each cavity using piezoelectric actuators, or in other similar schemes, as described in the previous sections.

Figure 10(c) presents a comparison among the band diagrams of such a photonic crystal with and without modulation. Without modulation (blue curves), four propagating bands are found near 22 kHz, two of which appear to be slow in nature corresponding to deaf modes, while the other two correspond to fast Dirac bands with degeneracy at both the G and K points. On the other hand, when the modulation is turned on (orange curves), the band diagram folds with a periodicity equal to the modulation frequency, as would be expected from the Floquet–Bloch theorem. More importantly, because the modulation breaks the temporal symmetry, the degeneracy at both the G and K points is lifted and a bandgap opens. The authors in [81] theoretically predicted the existence of a unidirectional edge state in such a gap by calculating the topological invariant of the first Chern class for the four conduction bands. Such a prediction was then validated through the full-wave simulations of a truncated lattice, confirming the theoretical analysis.

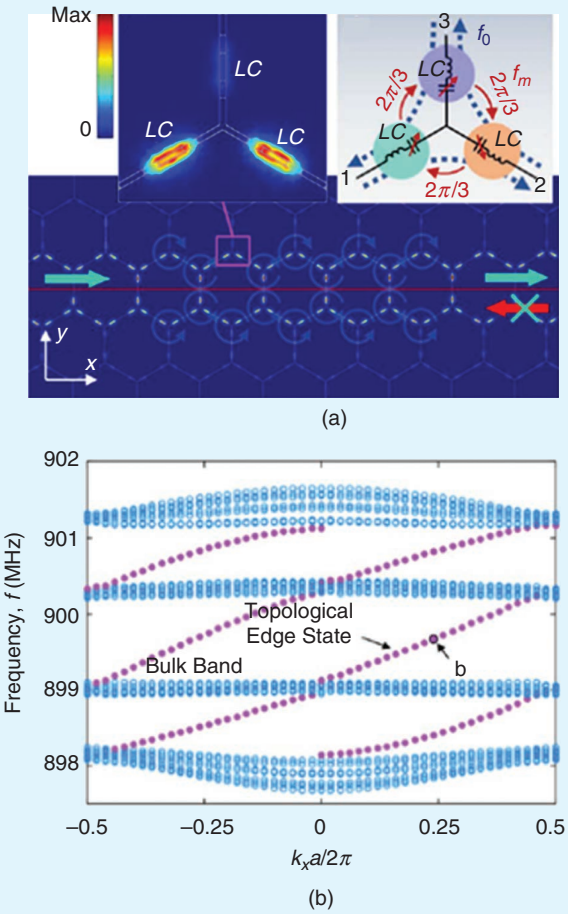

FIGURE 11. (a) The hexagonal lattice consisting of electronic STM-AM circulators based on the bandpass/wye topology of Figure 2(a) [85]. An artificial boundary is created at the middle of two domains inside the lattice, each with an opposite direction of STM-AM bias. The schematic and energy density of a single meta-atom near the artificial interface are shown in the insets. (b) The band diagram with four conduction bands (blue) and a topologically protected edge state (purple) at the artificial interface.

In [85], an electronic STM-AM TI was also presented. Similar to the TI shown in Figure 10, the lattice was also hexagonal but the meta-atom was based on a bandpass/wye STM-AM circulator, as depicted in Figure 4(a). Without modulation, the lattice exhibits a continuous energy spectrum with six Dirac points. When STM-AM biasing is applied to each meta-atom, the degeneracy of the Dirac points is lifted and a bandgap opens in the bulk. Furthermore, to test for the presence of an edge mode, the lattice can be divided it into two regions, one with a clockwise STM-AM bias and the other with a counterclockwise bias. Such a division results in a domain wall between the two regions that can support an edge state and is easier to calculate numerically. Figure 11(a) shows the spatial distribution of the energy density of such a mode when excited at the middle of the bandgap. As depicted in Figure 11(a), the energy is localized around the artificial boundary and decays sharply in the bulk. Figure 11(b) shows the band diagram for such a scenario, which indeed manifests an edge mode that can carry energy only in the $+x$ direction. An experimental demonstration for elastic waves has also been recently reported using arrays of piezoelectric elements [82], also showing dynamic reconfigurability and opportunities for multiplexing.

STM-AM Floquet TIs do not require fast modulation speeds nor phase uniformity among different unit cells, which eases their implementation and makes them relevant for practical applications, for instance, for multiplexing. The channels can be dynamically reconfigured thanks to the possibility of creating artificial domain walls by simply controlling the direction of the STM-AM bias, which is of significant importance in today's programmable systems. This, in turn, opens the door to new venues and possibilities in future research directions.

CONCLUSIONS

In this article, we reviewed the concept and recent progress of magnet-free STM-AM devices. We outlined the underlying physical principles and presented their basic topologies and advanced architectures, with a focus on a single-device element to realize the circulators. For completeness, the results of all the fabricated prototypes are summarized in Table 2. We also provided an outlook on the potential impact STM-AM circulators may have on future technologies, including wireless full-duplex communications, and in the field of metamaterials, such as Floquet TIs. The antennas and propagation community can play a pivotal role in pushing forward application research on these systems, in which many outstanding challenges remain, both from a modeling and theoretical perspective, for instance, in the efficient calculation of time-modulated systems, and from the practical and efficient implementation of these devices for various applications.

ACKNOWLEDGMENTS

This work was supported by a Qualcomm Innovation Fellowship, an IEEE Microwave Theory and Techniques Society Graduate Fellowship, the Air Force Office of Scientific Research, DARPA, Silicon Audio, the Simons Foundation, and the National Science Foundation. The corresponding author is Andrea Alù.

AUTHOR INFORMATION

Ahmed Kord (ahmed.kord@utexas.edu) is a senior engineer at Qualcomm Inc., San Diego, California, 92121, USA. He is a Forbes 30 Under 30 in Science alumnus. His current research interests include radio-frequency integrated circuits and biomedical systems.

Andrea Alù (alu@mail.utexas.edu) is the founding director of the Photonics Initiative at the City University of New York (CUNY), New York, 10031, USA, Advanced Science Research Center. He is also the Einstein Professor of Physics at the CUNY Graduate Center, 10016, a professor of electrical engineering at the City College of New York, 10031, USA, and an adjunct professor and senior research scientist at The University of Texas at Austin, Austin, Texas, 78705, USA. Currently, he is the CTO of Silicon Audio RF Circulator. He is a Fellow of IEEE. The terms of this arrangement have been reviewed and approved by The University of Texas at Austin and the City University of New York in accordance with their policy on objectivity in research. His research interests include metamaterials and plasmonics, electromagnetics, optics and nanophotonics, nanocircuits and nanostructures, and nanoantennas.

REFERENCES

[1] D. Korpi et al., "Full-duplex mobile device: Pushing the limits," *IEEE Commun. Mag.*, vol. 54, no. 9, pp. 80–87, Sept. 2016. doi: 10.1109/MCOM.2016.7565192.

[2] A. Sabharwal, P. Schniter, D. Guo, D. W. Bliss, S. Rangarajan, and R. Wichman, "In-band full-duplex wireless: Challenges and opportunities," *IEEE J. Sel. Areas Commun.*, vol. 32, no. 9, pp. 1637–1652, Sept. 2014. doi: 10.1109/JSAC.2014.2330193.

[3] J. I. Choi, M. Jain, K. Srinivasan, P. Levis, and S. Katti, "Achieving single channel, full duplex wireless communication," in *Proc. 16th Annu. Int. Conf. Mobile Comput. Netw.*, Chicago, Sept. 2010, pp. 1–12.

[4] M. Duarte, C. Dick, and A. Sabharwal, "Experiment-driven characterization of full-duplex wireless systems," *IEEE Trans. Wireless Commun.*, vol. 11, no. 12, pp. 4296–4307, Dec. 2012. doi: 10.1109/TWC.2012.102612.111278.

[5] A. Kord, D. L. Sounas, and A. Alù, "Achieving full-duplex communication: Magnetless parametric circulators for full-duplex communication systems," *IEEE Microw. Mag.*, vol. 19, no. 1, pp. 84–90, Jan. 2018. doi: 10.1109/MMM.2017.2759638.

[6] B. Debaillie et al., "Analog/RF solutions enabling compact full-duplex radios," *IEEE J. Sel. Areas Commun.*, vol. 32, no. 9, pp. 1662–1673, Sept. 2014. doi: 10.1109/JSAC.2014.2330171.

[7] J. Zhou et al., "Integrated full duplex radios," *IEEE Commun. Mag.*, vol. 55, no. 4, pp. 142–151, Apr. 2017. doi: 10.1109/MCOM.2017.1600583.

[8] M. Jain et al., "Practical, real-time, full duplex wireless," in *Proc. 17th Annu. Int. Conf. Mobile Comput. Netw.*, Las Vegas, NV, Sept. 2011, pp. 301–312.

[9] D. Bharadia et al., "Full duplex radios," *ACM SIGCOMM Comput. Commun. Rev*, vol. 43, no. 4, pp. 375–386, Sept. 2013. doi: 10.1145/2534169.2486033.

[10] D. M. Pozar, *Microwave Engineering*. Hoboken, NJ: Wiley, 2009.

[11] A. Kord, D. L. Sounas, and A. Alù, "Microwave nonreciprocity," *Proc. IEEE*, vol. 108, no. 10, pp. 1728–1758, 2020. doi: 10.1109/JPROC.2020.3006041.

[12] N. Reiskarimian, A. Nagulu, T. Dinc, and H. Krishnaswamy, "Nonreciprocal electronic devices: A hypothesis turned into reality," *IEEE Microw. Mag.*, vol. 20, no. 4, pp. 94–111, 2019. doi: 10.1109/MMM.2019.2891380.

[13] C. Caloz and A. Sihvola, "Electromagnetic chirality, part 1: The microscopic perspective [electromagnetic perspectives]," *IEEE Antennas Propag. Mag.*, vol. 62, no. 1, pp. 58–71, 2020. doi: 10.1109/MAP.2019.2955698.

[14] S. Taravati and A. A. Kishk, "Space-time modulation: Principles and applications," *IEEE Microw. Mag.*, vol. 21, no. 4, pp. 30–56, 2020. doi: 10.1109/MMM.2019.2963606.

[15] J. A. Weiss, N. G. Watson, and G. F. Dionne, "New uniaxial-ferrite millimeter-wave junction circulators," in *Proc. Int. Symp. IEEE MTT-S Microw.*, Long Beach, CA, 1989, vol. 1, pp. 145–148.

[16] A. Saib, M. Darques, L. Piraux, D. Vanhoenacker-Janvier, and I. Huynen, "Unbiased microwave circulator based on ferromagnetic nanowires arrays of tunable magnetization state," *J. Phys. D, Appl. Phys.*, vol. 38, no. 16, pp. 2759–2763, Aug. 2005. doi: 10.1088/0022-3727/38/16/003.

[17] L. P. Carignan, A. Yelon, D. Menard, and C. Caloz, "Ferromagnetic nanowire metamaterials: Theory and applications," *IEEE Trans. Microw. Theory Techn.*, vol. 59, no. 10, pp. 2568–2586, Oct. 2011. doi: 10.1109/TMTT.2011.2163202.

[18] S. A. Oliver et al., "Integrated self-biased hexaferrite microstrip circulators for millimeter-wavelength applications," *IEEE Trans. Microw. Theory Techn*, vol. 49, no. 2, pp. 385–387, 2001. doi: 10.1109/22.903102.

[19] J. Wang et al., "Self-biased Y-junction circulator at Ku band," *IEEE Microw. Wireless Compon. Lett*, vol. 21, no. 6, pp. 292–294, 2011. doi: 10.1109/LMWC.2011.2142297.

[20] S. Tanaka, N. Shimomura, and K. Ohtake, "Active circulators: The realization of circulators using transistors," *Proc. IEEE*, vol. 53, no. 3, pp. 260–267, 1965. doi: 10.1109/PROC.1965.3683.

[21] A. W. Keen, J. L. Glover, and R. J. Harris, "Realisation of the circulator concept using differential-input operational amplifiers," *Electron. Lett.*, vol. 4, no. 18, pp. 389–391, Sept. 1968. doi: 10.1049/el:19680307.

[22] T. Kodera, D. L. Sounas, and C. Caloz, "Magnetless nonreciprocal metamaterial (MNM) technology: Application to microwave components," *IEEE Trans. Microw. Theory Techn.*, vol. 61, no. 3, pp. 1030–1042, Mar. 2013. doi: 10.1109/TMTT.2013.2238246.

[23] T. Kodera, D. L. Sounas, and C. Caloz, "Artificial Faraday rotation using a ring metamaterial structure without static magnetic field," *Appl. Phys. Lett.*, vol. 99, no. 3, July 2011. doi: 10.1063/1.3615688.

[24] S. Wang, C. H. Lee, and Y. B. Wu, "Fully integrated 10-GHz active circulator and quasi-circulator using bridged-T networks in standard CMOS," *IEEE Trans. Very Large Scale Integr. (VLSI) Syst.*, vol. 24, no. 10, pp. 3184–3192, Oct. 2016. doi: 10.1109/TVLSI.2016.2535377.

[25] C.-H. Chang, Y.-T. Lo, and J.-F. Kiang, "A 30 GHz active quasicirculator with current-reuse technique in 0.18 μm CMOS technology," *IEEE Microw. Wireless Compon. Lett.*, vol. 20, no. 12, pp. 693–695, Dec. 2010. doi: 10.1109/LMWC.2010.2079321.

[26] G. Carchon and B. Nanwelaers, "Power and noise limitations of active circulators," *IEEE Trans. Microw. Theory Techn.*, vol. 48, no. 2, pp. 316–319, Feb. 2000. doi: 10.1109/22.821785.

[27] P. Aleahmad, M. Khajavikhan, D. Christodoulides, and P. LiKamWa, "Integrated multi-port circulators for unidirectional optical information transport," *Sci. Rep.*, vol. 7, no. 1, 2017, Art. no. 2129. doi: 10.1038/s41598-017-02340-9.

[28] K. Y. Yang et al., "Inverse-designed photonic circuits for fully passive, bias-free Kerr-based nonreciprocal transmission and routing," *Nat. Photonics*, vol. 14, pp. 369–374, Mar. 2020. doi: 10.1038/s41566-020-0606-0.

[29] G. D'Aguanno, D. L. Sounas, H. M. Sayed, and A. Alù, "Nonlinearity-based circulator," *Appl. Phys. Lett.*, vol. 114, no. 18, May 7, 2019, Art. no. 181102. doi: 10.1063/1.5094736.

[30] D. L. Sounas, C. Caloz, and A. Alù, "Giant non-reciprocity at the subwavelength scale using angular momentum-biased metamaterials," *Nat. Commun.*, vol. 4, Sept. 2013, Art. no. 2407. doi: 10.1038/ncomms3407.

[31] N. A. Estep et al., "Magnetic-free non-reciprocity and isolation based on parametrically modulated coupled-resonator loops," *Nat. Phys.*, vol. 10, no. 12, pp. 923–927, Nov. 2014. doi: 10.1038/nphys3134.

[32] N. A. Estep, D. L. Sounas, and A. Alù, "Magnetless microwave circulators based on spatiotemporally modulated rings of coupled resonators," *IEEE Trans. Microw. Theory Techn.*, vol. 64, no. 2, pp. 502–518, Feb. 2016.

[33] A. Kord, D. L. Sounas, and A. Alù, "Magnetless circulators based on spatio-temporal modulation of bandstop filters in a delta topology," *IEEE Trans. Microw. Theory Techn.*, vol. 66, no. 2, pp. 911–926, Feb. 2018. doi: 10.1109/TMTT.2017.2757470.

[34] A. Kord, D. L. Sounas, and A. Alù, "Pseudo-linear time-invariant magnetless circulators based on differential spatio-temporal modulation of resonant junctions," *IEEE Trans. Microw. Theory Techn.*, vol. 66, no. 6, pp. 2731–2745, June 2018. doi: 10.1109/TMTT.2018.2818152.

[35] A. Kord, H. Krishnaswamy, and A. Alù, "Magnetless circulators with harmonic rejection based on N-way cyclic-symmetric time-varying networks," *Phys. Rev. Appl.*, vol. 12, no. 2, Aug. 2019, Art. no. 024046. doi: 10.1103/PhysRevApplied.12.024046.

[36] A. Kord, D. L. Sounas, Z. Xiao, and A. Alù, "Broadband cyclic-symmetric magnet-less circulators and theoretical bounds on their bandwidth," *IEEE Trans. Microw. Theory Techn.*, vol. 66, no. 12, pp. 5472–5481, Dec. 2018. doi: 10.1109/TMTT.2018.2860023.
[37] A. Kord, M. Tymchenko, D. L. Sounas, H. Krishnaswamy, and A. Alù, "CMOS integrated magnetless circulators based on spatiotemporal modulation angular-momentum biasing," *IEEE Trans. Microw. Theory Techn.*, vol. 67, no. 7, pp. 2649–2662, July 2019. doi: 10.1109/TMTT.2019.2915074.
[38] C. Yang and P. Gui, "85–110-GHz CMOS magnetic-free nonreciprocal components for full-duplex transceivers," *IEEE J. Solid-State Circuits*, vol. 54, no. 2, pp. 368–379, 2018. doi: 10.1109/JSSC.2018.2875478.
[39] C. Cassella et al., "Radio frequency angular momentum biased quasi-LTI nonreciprocal acoustic filters," *IEEE Trans. Ultrason. Ferroelectr. Freq. Control (UFFC)*, vol. 66, no. 11, pp. 1814–1825, July 2019. doi: 10.1109/TUFFC.2019.2931121.
[40] Y. Yu et al., "Radio frequency magnet-free circulators based on spatiotemporal modulation of surface acoustic wave filters," *IEEE Trans. Microw. Theory Techn*, vol. 67, no. 12, pp. 4773–4782, 2019. doi: 10.1109/TMTT.2019.2943291.
[41] Y. Yu et al., "Highly-linear magnet-free microelectromechanical circulators," *IEEE J. Microelectromech. Syst. (MEMS)*, vol. 28, no. 6, pp. 933–940, Dec. 2019. doi: 10.1109/JMEMS.2019.2947903.
[42] D. L. Sounas, N. A. Estep, A. Kord, and A. Alù, "Angular-momentum biased circulators and their power consumption," *IEEE Antennas Wireless Propag. Lett.*, vol. 17, no. 11, pp. 1963–1967, Nov. 2018. doi: 10.1109/LAWP.2018.2868790.
[43] A. Kord, D. L. Sounas, and A. Alù, "Differential magnetless circulator using modulated bandstop filters," in *Proc. IEEE MTT-S Int. Microw. Symp. (IMS) Dig*, Honolulu, HI, June 2017, pp. 384–387. doi: 10.1109/MWSYM.2017.8058574.
[44] A. Kord, D. L. Sounas, and A. Alù, "Low-loss broadband magnetless circulators for full-duplex radios," in *Proc. IEEE MTT-S Int. Mircow. Symp. (IMS)*, Philadelphia, June 2018, pp. 506–509. doi: 10.1109/MWSYM.2018.8439849.
[45] S. Qin, Q. Xu, and Y. E. Wang, "Nonreciprocal components with distributedly modulated capacitors," *IEEE Trans. Microw. Theory Techn.*, vol. 62, no. 10, pp. 2260–2272, Oct. 2014. doi: 10.1109/TMTT.2014.2347935.
[46] N. Reiskarimian and H. Krishnaswamy, "Magnetic-free non-reciprocity based on staggered commutation," *Nat. Commun.*, vol. 7, Apr. 2016, Art. no. 11217. doi: 10.1038/ncomms11217.
[47] N. Reiskarimian, J. Zhou, and H. Krishnaswamy, "A CMOS passive LPTV non-magnetic circulator and its application in a full-duplex receiver," *IEEE J. Solid-State Circuits*, vol. 52, no. 5, pp. 1358–1372, May 2017. doi: 10.1109/JSSC.2017.2647924.
[48] T. Dinc et al., "Synchronized conductivity modulation to realize broadband lossless magnetic-free non-reciprocity," *Nat. Commun.*, vol. 8, no. 1, Oct. 2017, Art. no. 795. doi: 10.1038/s41467-017-00798-9.
[49] A. Nagulu, A. Alù, and H. Krishnaswamy, "Fully-integrated non-magnetic 180nm SOI circulator with >1W P1dB, >+50dBm IIP3 and high isolation across 1.85 VSWR," in *IEEE Radio Freq. Integ. Circuits Symp. (RFIC)*, Philadelphia, June 2018, pp. 104–107. doi: 10.1109/RFIC.2018.8428969.
[50] M. M. Biedka et al., "Ultra-wide band non-reciprocity through sequentially-switched delay lines," *Sci. Rep.*, vol. 7, no. 1, Jan. 2017, Art. no. 40014. doi: 10.1038/srep40014.
[51] M. M. Biedka, R. Zhu, Q. M. Xu, and Y. E. Wang, "Ultra-wide band on-chip circulators for full-duplex communications," *Proc. IEEE/MTT-S Int. Microwave Symp*, 2018, pp. 987–990.
[52] C. Xu, E. Calayir, and G. Piazza, "Magnetic-free electrical circulator based on AlN MEMS filters and CMOS RF switches," in *Proc. 31st IEEE Int. Conf. Micro Electro-Mech. Syst. (MEMS 2018)*, Belfast, U.K., Jan. 2018, pp. 755–758.
[53] Y. Yu et al., "Magnetic-free radio frequency circulator based on spatiotemporal commutation of MEMS resonators," in *Proc. 31st IEEE Int. Conf. Micro Electro-Mech. Syst. (MEMS 2018)*, Belfast, U.K., Jan. 2018, pp. 154–157.
[54] Y. Yu et al., "2.5 GHz highly-linear magnetic-free microelectromechanical resonant circulator," in *Proc. IEEE Int. Freq. Cont. Symp. (IFCS 2018)*, Olympic Valley, CA, May 2018.
[55] M. M. Torunbalci, T. J. Odelberg, S. Sridaran, R. C. Ruby, and S. A. Bhave, "An FBAR circulator," *IEEE Microw. Wireless Compon. Lett.*, vol. 28, no. 5, pp. 395–397, May 2018. doi: 10.1109/LMWC.2018.2815271.
[56] R. Fleury, D. L. Sounas, C. F. Sieck, M. R. Haberman, A. Alù, "Sound isolation and giant linear nonreciprocity in a compact acoustic circulator," *Science*, vol. 343, no. 6170, pp. 516–519, Jan. 2014. doi: 10.1126/science.1246957.
[57] Z. Yu and S. Fan, "Complete optical isolation created by indirect interband photonic transitions," *Nat. Photon.*, vol. 3, no. 2, pp. 91–94, Feb. 2009. doi: 10.1038/nphoton.2008.273.
[58] H. Lira, Z. Yu, S. Fan, and M. Lipson, "Electrically driven nonreciprocity induced by interband photonic transition on a silicon chip," *Phys. Rev. Lett.*, vol. 109, no. 3, July 2012. Art. no. 033901. doi: 10.1103/PhysRevLett.109.033901.
[59] K. Fang, Z. Yu, and S. Fan, "Photonic Aharonov–Bohm effect based on dynamic modulation," *Phys. Rev. Lett.*, vol. 108, no. 15, Apr. 2012. Art. no. 153901. doi: 10.1103/PhysRevLett.108.153901.
[60] A. Kamal, J. Clarke, and M. H. Devoret, "Noiseless non-reciprocity in a parametric active device," *Nat. Phys.*, vol. 7, no. 4, pp. 311–315, Apr. 2011. doi: 10.1038/nphys1893.
[61] J. Kerckhoff, K. Lalumière, B. J. Chapman, A. Blais, and K.W. Lehnert, "On-chip superconducting microwave circulator from synthetic rotation," *Phys. Rev. Appl.*, vol. 4, no. 3, Sept. 2015, Art. no. 034002.
[62] K. M. Sliwa et al., "Reconfigurable Josephson circulator/directional amplifier," *Phys. Rev. X*, vol. 5, no. 4, Nov. 2015, Art. no. 041020. doi: 10.1103/PhysRevX.5.041020.
[63] F. Lecocq et al., "Nonreciprocal microwave signal processing with a field-programmable Josephson amplifier," *Phys. Rev. Appl.*, vol. 7, no. 2, Feb. 2017, Art. no. 024028.
[64] A. M. Mahmoud, A. R. Davoyan, and N. Engheta, "All-passive nonreciprocal metastructure," *Nat. Commun.*, vol. 6, no. 8359, July 2015.
[65] R. Duggan, D. L. Sounas, and A. Alù, "Optically driven effective Faraday effect in instantaneous nonlinear media," *Optica*, vol. 6, no. 9, pp. 1152–1157, Aug. 30, 2019. doi: 10.1364/OPTICA.6.001152.
[66] J. E. Moore, "The birth of topological insulators," *Nature*, vol. 464, no. 7286, pp. 194–198, Mar. 2010. doi: 10.1038/nature08916.
[67] M. Z. Hasan and C. L. Kane, "Colloquium: Topological insulators," *Rev. Mod. Phys.*, vol. 82, no. 4, pp. 3045–3067, Nov. 2010. doi: 10.1103/RevModPhys.82.3045.
[68] Z. Wang, Y. Chong, J. D. Joannopoulos, and M. Soljačić, "Observation of unidirectional backscattering-immune topological electromagnetic states," *Nature*, vol. 461, no. 7265, pp. 772–775, Oct. 2009. doi: 10.1038/nature08293.
[69] L. Lu, J. D. Joannopoulos, and M. Soljačić, "Topological photonics," *Nat. Photon.*, vol. 8, no. 11, pp. 821–829, Oct. 2014. doi: 10.1038/nphoton.2014.248.
[70] R. O. Umucalılar and I. Carusotto, "Artificial gauge field for photons in coupled cavity arrays," *Phys. Rev. A*, vol. 84, no. 4, Oct. 2011. doi: 10.1103/PhysRevA.84.043804.
[71] M. I. Shalaev, S. Desnavi, W. Walasik, and N. M. Litchinitser, "Reconfigurable topological photonic crystal," *New J. Phys.*, vol. 20, no. 2, Feb. 2018, Art. no. 023040. doi: 10.1088/1367-2630/aaac04.
[72] Q. Lin, X.-Q. Sun, M. Xiao, S.-C. Zhang, and S. Fan, "A three-dimensional photonic topological insulator using a two-dimensional ring resonator lattice with a synthetic frequency dimension," *Science Adv.*, vol. 4, no. 10, Oct. 2018, Art. no. eaat2774. doi: 10.1126/sciadv.aat2774.
[73] K. Fang, Z. Yu, and S. Fan, "Realizing effective magnetic field for photons by controlling the phase of dynamic modulation," *Nat. Photon.*, vol. 6, no. 11, pp. 782–787, Oct. 2012. doi: 10.1038/nphoton.2012.236.
[74] M. Hafezi, S. Mittal, J. Fan, A. Migdall, and J. M. Taylor, "Imaging topological edge states in silicon photonics," *Nat. Photon.*, vol. 7, no. 12, pp. 1001–1005, Dec. 2013. doi: 10.1038/nphoton.2013.274.
[75] M. Pasek and Y. D. Chong, "Network models of photonic Floquet topological insulators," *Phys. Rev. B*, vol. 89, no. 7, Feb. 2014, Art. no. 075113. doi: 10.1103/PhysRevB.89.075113.
[76] W.-J. Chen et al., "Experimental realization of photonic topological insulator in a uniaxial metacrystal waveguide," *Nat. Commun.*, vol. 5, no. 1, Dec. 2014, Art. no. 5782.
[77] T. Ma, A. B. Khanikaev, S. H. Mousavi, and G. Shvets, "Guiding electromagnetic waves around sharp corners: topologically protected photonic transport in metawaveguides," *Phys. Rev. Lett.*, vol. 114, no. 12, Mar. 2015, Art no. 127401. doi: 10.1103/PhysRevLett.114.127401.
[78] X. Cheng, C. Jouvaud, X. Ni, S. H. Mousavi, A. Z. Genack, and A. B. Khanikaev, "Robust reconfigurable electromagnetic pathways within a photonic topological insulator," *Nat. Mater.*, vol. 15, pp. 1–8, Feb. 2016.
[79] X. Ni, M. Weiner, A. Alù, and A. B. Khanikaev, "Observation of higher-order topological acoustic states protected by generalized chiral symmetry," *Nat. Mater.*, vol. 18, no. 2, pp. 113–120, Feb. 2019. doi: 10.1038/s41563-018-0252-9.
[80] A. B. Khanikaev, R. Fleury, S. H. Mousavi, and A. Alù, "Topologically robust sound propagation in an angular-momentum-biased graphene-like resonator lattice," *Nat. Commun.*, vol. 6, no. 1, Dec. 2015, Art. no. 8260.
[81] R. Fleury, A. B. Khanikaev, and A. Alù, "Floquet topological insulators for sound," *Nat. Commun*, vol. 7, June 2016, Art. no. 11744. doi: 10.1038/ncomms11744.
[82] A. Darabi, X. Ni, M. Leamy, and A. Alù, "Reconfigurable Floquet elastodynamic topological insulators based on synthetic angular momentum bias," *Sci. Adv.*, vol. 6, no. 29, July 2020, Art. no. eaba8656. doi: 10.1126/sciadv.aba8656.

[83] C. H. Lee et al., "Topolectrical circuits," *Commun. Phys.*, vol. 1, no. 1, Dec. 2018, Art. no. 39.
[84] S. Imhof et al., "Topolectrical-circuit realization of topological corner modes," *Nat. Phys.*, vol. 14, no. 9, pp. 925–929, Sept. 2018. doi: 10.1038/s41567-018-0246-1.
[85] M. Tymchenko and A. Alù, "Circuit-based magnetless Floquet topological insulator," in *Proc. 10th Int. Congr. Adv. Electromagn. Mater. Microw. Optics (METAMATERIALS)*, 2016.